Facet Dependent Catalytic Activity of Pd Nanocrystals for the Remedy of Organic Pollutant: A Mechanistic Study

Swarnalata Swain,[a] Bhamy Maithry Shenoy,[b] Prangya Bhol,[a] Sudesh Yadav,[c] Satya Ranjan Jena,[a] Gopalkrishna Hegde,[b] Ali Altaee,[c] Manav Saxena,[a] Akshaya K. Samal[a]*

[a]Centre for Nano and Material Sciences, Jain University, Jain Global Campus, Ramanagara, Bangalore - 562112, India

[b]Centre for Biosystems Science and Engineering, Indian Institute of Science, Bangalore – 560012, India

[c]Centre for Green Technology, School of Civil and Environmental Engineering, University of Technology Sydney, 15 Broadway, NSW 2007, Australia

Email: s.akshaya@jainuniversity.ac.in

Abstract

The facet effect and underlying molecular mechanisms of noble metal-based nanocrystals have shown promise as a potential candidate for various applications including catalysis and soil-water remediation. Facet-dependent catalytic activities of Palladium (Pd) nanocrystals have great significance in the field of catalysis. In this report, the well-known seed-mediated synthesis method has been used to synthesize three different Pd nanostructures of cuboctahedral (Coh), octahedral (Oh), and nanocubes (NCs). By changing the time and temperature, the growth of nanocrystals was directed along different low index planes such as {100} for NCs, {111} for Oh, and mixed planes of {100} and {111} for Coh structures. Shape-controlled Pd nanocrystals with distinctly varied surface facets were used to conduct a mechanistic study for the remediation of organic dyes. To understand the facets dependent catalysis, nanocrystals were employed for the reduction of organic pollutant 4-Nitroaniline (4-NA) to 4-Phenylenediamine (4-PDA), and the substituent effect of nitro ($-NO_2$) groups were studied. By keeping the total surface area of particles unchanged, different volumes of nanocrystals were taken into account to carry out an accurate facet-dependent analysis. Further to extend the catalytic activity study, degradation of cationic dye, Rhodamine B (Rh B), and anionic dye, Methyl Orange (MO) were performed. The reduction and degradation processes were monitored through UV-Visible absorption spectroscopy. It was confirmed from the absorption spectra that the efficiency of Pd NCs was higher than Oh and Coh nanocrystals, which established the depiction of the best role of {100} plane out of the other two

planes exposed on the surface. The catalytic trends for the asymmetric growth of planes follows the order of NCs {100}> Oh {111}> Coh {100} {111}. The specific reactivity performance of the nanocrystals was confirmed using an analytical model.

Keywords: Palladium nanocrystals; Low index planes; Organic pollutant; Cationic dye and Anionic dye

1. Introduction

Active site modification of noble metal nanocrystals has recently attracted considerable attention in catalysis. The word "nanocrystal" rather than "nanoparticle" highlights the formation of crystalline lattices along certain facets [1-4]. Size, shape, and composition-dependent catalytic activities of nanocrystals have been witnessed in earlier reports [5-10]. By fine-tuning the above-mentioned parameters, the catalytic activity of a nanomaterial can be enhanced [11-17]. Recently, the research field of anisotropic nanocrystals is focused on the role of different facets on the surface. Noble metal nanocrystals such as Platinum (Pt), Gold (Au), Palladium (Pd), and Silver (Ag) having various low index facets such as {111}, {100} and {110} exhibit   different chemical reactivities/selectivities due to the presence of different surface atom densities [18-22]. Bratlie et al. reported that hydrogenation of benzene in presence of Pt cuboctahedrons that exposed {111} and {100} facets yielded both cyclohexane and cyclohexene. In contrast, only cyclohexene is formed as a product when only {100} facets [23] are present. Chiu et al. described hydrogenation of 4-NA catalyzed by Au rhombic dodecahedra {110}, cube {100} and octahedra {111}. The catalytic activity for reduction reaction follows the order of {110} > {100} > {111} for the temperature range between 25 to 36 °C. However, when the temperature is increased to 40 °C, Au octahedra {111} showed better catalytic activity over the cube {100} [24].

The geometry, selectivity, and facet dependent catalytic activity have also been studied for various applications [25-31]. Several approaches are employed for the synthesis of anisotropic nanostructures having different active facets. Some of the methods are one-pot synthesis, template-assisted synthesis, electrochemical synthesis, polyol, photochemical synthesis, etc [32-35]. In the procedures mentioned above, the main concern is to understand the importance of using organic solvents and establishing proper mechanisms and stability. However, an aqueous medium seed-mediated synthesis provides better control over the size, uniformity, shape evolution of metal

nanostructures, and also offers high yield [36,37]. It includes two steps i) nucleation of seed particles with the desired shape, ii) growth of the metal atom upon the surface of seed to get precise structures [38]. The concentration of precursors, the role of surfactant, capping agent, and insertion of additives play an important role in the growth of different facets of nanocrystals [39-46]. A seeded growth method of Pd nanocrystals has been reported, in which formaldehyde and potassium iodide acted as shape directing agents that controlled shapes of different proportions of low index facets [47,48]. Pd has attracted considerable research interest due to its unique property of change in stable oxidation state (0, +2) and can be a good replacement for Platinum (Pt) in many industrial applications. Some of the notable examples are exceptional performance in hydrogen storage and hydrogen sensing, [49,50]. Pd performed as an effective catalyst and yielded useful biaryls in various C-C bond forming reactions like Stille, Suzuki-Miyaura, Hiyama, and Heck coupling [51-54]. Facet dependent catalytic activity of Pd nanostructures was recently studied by Laskar and Skrabalak [55]. They carried out hydrogenation of 2-hexyne using Pd cubes and octahedral and observed that octahedra exhibited better performance compared to cubes. This is because Pd (100) surface of cubes binds alkynes more strongly than Pd (111) surface of octahedra [55].

Nitro substituted aniline and dyes are used in many industrial productions. Human exposure to nitro compounds causes symptoms like headaches, drowsiness, nausea, and cyanosis. Due to the high solubility and stability of these organic pollutants in water, they generate antagonistic results for aquatic organisms. Hence, it is imperative to create a suitable path to avoid the effect of these hazardous chemicals [56]. The catalytic activity of precious metal atoms mainly depends upon the active metal atoms on the surface. Mainly the activity depends upon the specific surface area of the materials. Therefore designing suitable active materials for the reduction and degradation of water contaminants is more helpful [57-61]. In this study, optimization of the temperature and time leads to provide three different anisotropic structural growth along the low index planes such as {100} for NCs, {111} for Oh and mixed growth of {100} and {111} for Coh. Synthesized Pd nanocrystals were employed to reduce different NA to respective PDA and the degradation of cationic and anionic dyes was studied.

2. Experimental

2.1. Materials and methods

Palladium (II) chloride (PdCl$_2$, 99%), Cetyltrimethylammonium bromide (CTAB, 98%), Sodium borohydride (NaBH$_4$, > 98%), concentrated hydrochloric acid (HCl, > 98%) and Methyl orange (MO, >85%) were purchased from SD Fine Chemical Limited, India. Ascorbic acid (L-AA, 99%) and Rhodamine B (RhB, > 90%) were purchased from Merck. NA derivatives (4-NA, 3-NA, and 2-NA) were purchased from Sigma Aldrich. All the above chemicals were used without further purification. Distilled water was utilized for the preparation of solution and reaction purposes. All the glassware was thoroughly cleaned with aqua regia and finally rinsed with distilled water.

The absorption study was performed with UV-Visible spectrophotometer PerkinElmer Lambda 360 instrument. Field Emission Scanning Electron Microscopy (FESEM) performance was carried out with the instrument JEOL, Singapore. TEM and HRTEM analyses were done using Thermo Scientific TALOS F200S G2 (200 KV), FEG, CMOS Camera 4K x 4K. Samples for HRTEM were carried out by drop-casting on 300 mesh carbon-coated copper grid. Powder X-ray diffraction (PXRD) patterns were achieved on Rigaku X-ray diffraction Ultima-IV, Japan using Cu Kα radiation source with a scan rate of 2 deg min^{-1} and 2θ ranges from 10 to 80 °.

2.2. Synthesis of Pd Coh, Oh, and NCs.

2.2.1. Preparation of Pd seed

All the three Pd nanocrystals were synthesized using seed-mediated synthesis protocol reported elsewhere with modification in the temperature and growth time [56,36]. Initially, H$_2$PdCl$_4$ (20 mM) solution was prepared by the addition of 0.115 g of PdCl$_2$ with 6.5 mL 0.2 M concentration (conc.) HCl and stirred for 3 hours (h) to acquire an orange solution of H$_2$PdCl$_4$. Further, it was diluted with water to form 20 mM of H$_2$PdCl$_4$ solution. Seed solution was synthesized by dissolving 0.045 g of CTAB in 10 mL of distilled water and heated up to 95 °C with vigorous stirring for 5-10 min in a round bottom flask. After observing a clear solution, 0.25 mL of H$_2$PdCl$_4$ was added subsequently, following the addition of 0.02 mL of L-AA (0.4 M) solution. After 10 min of continuous stirring, the color of the solution was changed to blackish brown, and later the solution was cooled to room temperature and allowed for ageing up to 2 h without disturbance for the proper growth of seed particles.

2.2.2. Preparation of growth solution

Three growth solutions were prepared by taking 9.0 g of CTAB and 90 mL of distilled water in each and then vigorously stirred for 15 min at three different temperatures 35 °C, 55 °C, and 70 °C to get different morphologies. 3.2 mL of 20 mM H_2PdCl_4 precursor was added to each. A schematic representation of the formation of three different nanostructures is shown in Figure 1.
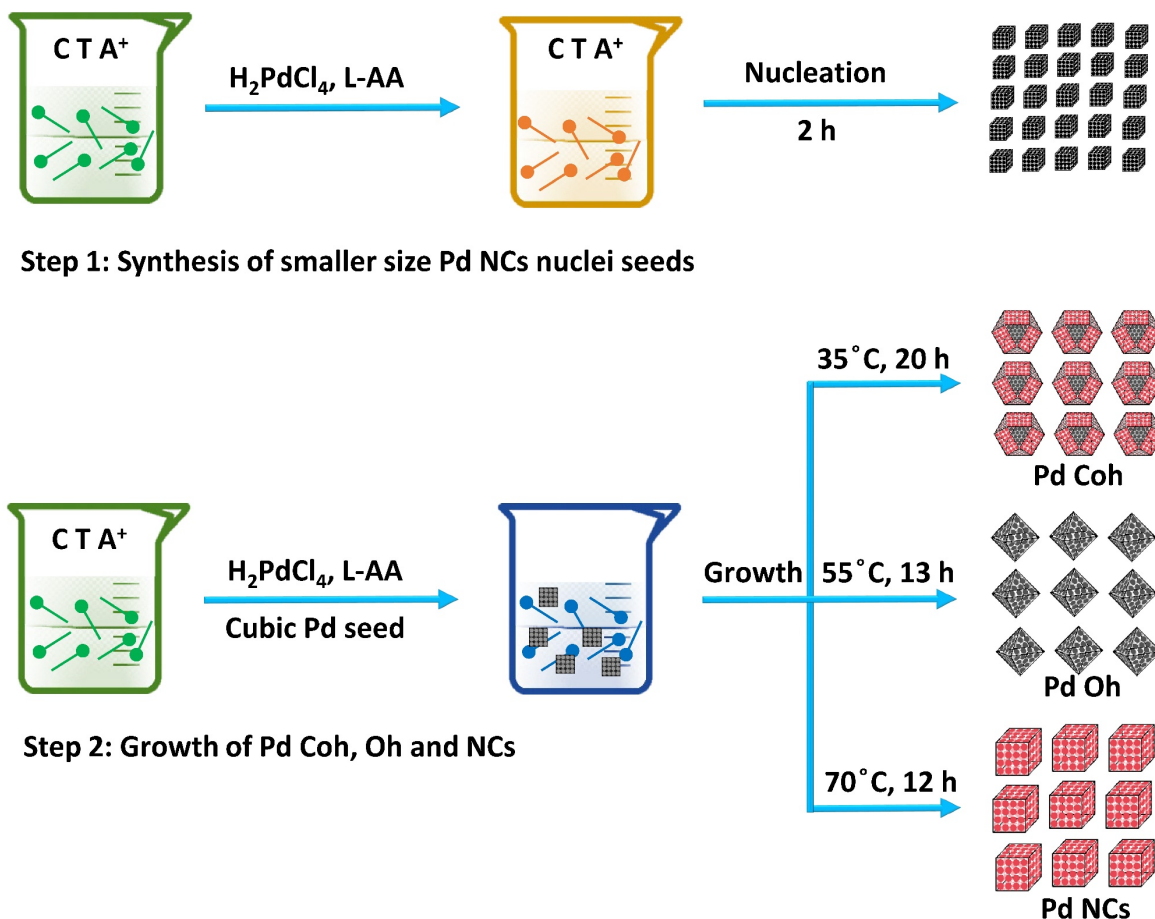

Figure 1. Schematic representation of synthesis steps involved during the formation of three different nanostructures.

Next, 2 mL of aged Pd seeds were added for the growth of the solution under vigorous stirring, followed by the addition of 2.5 mL of 0.4 M L-AA. The resulting reaction mixtures were kept undisturbed for 20 h, 13 h, and 12 h at 35 °C, 55 °C, and 70 °C, respectively. Pd nanocrystals were cooled down to room temperature, and nanostructures settled to the bottom of the flask. The growth solutions were sonicated for 1 min to remove the settled particles from the flask and were centrifuged two times at 6500 rpm for 15 min to eradicate the unreacted ions and excess surfactant.

The residue was redispersed in distilled water for further use. The samples were dried under ambient conditions for catalytic study.

2.3. Procedure for Reduction Reaction

2.3.1. Determination of Catalyst Concentration

To find the appropriate amount of catalyst loading, initially, 1 mg/mL Pd Oh catalyst was prepared. The reaction progress was observed by adding to reactant 4-NA to reduce 4-NA to 1, 4-PDA monitored by UV-Visible spectroscopy. The catalyst loading was optimized to 2 mg/mL for further study.

2.3.2. Standard catalysis experiments

To investigate the catalytic activities of respective facets present in Pd nanostructure, a typical reduction experiment was conducted, and the performance was monitored through UV-Visible spectroscopy. First, 0.001 M of 4-NA, 3-NA, 2-NA, and 0.1 M $NaBH_4$ aqueous solutions were prepared, and the reaction progress was preliminarily observed by adding different volumes of catalysts of different surface area. In a quartz cuvette, 200 μL 4-NA mixed with 2 mL of H_2O and 500 μL of freshly prepared ice-cold aqueous $NaBH_4$ solution was added. Different volumes of catalyst (2 mg/mL) were added to the reaction mixture, and the responses are observed by monitoring the absorption spectra.

2.3.3. Comparative catalysis experiment

After the catalytic reduction of different surface areas having the same volume of catalyst, the next varied volumes of a catalyst having the same surface area of ~5 cm^2 were calculated and used for the comparison study (details about surface area calculation is given in S1). 200 μL of 4-NA and 500 μL of $NaBH_4$ of the concentration mentioned above were taken and after that 15 μL of Coh, 26.5 μL Oh and 30 μL of Pd NCs were added to the mixture in three different reactions. When the reduction was completed, the catalysts were separated from the reaction mixture through centrifugation and washed with ethanol and water. The procedure outlined above was repeated for dye degradation, except that in place of NA, two different dyes were used and all other parameters remained constant.

3. Result and Discussion

3.1. Physicochemical characterization

The aqueous phase seed-mediated synthesis method was used to synthesize Pd nanocrystals with different facets using CTAB as the surface stabilizing agent, which prevents agglomeration and leaching out of metal atoms from the surface. Modification in temperature and growth time of the reaction mixture established the depiction of different Pd nanostructures on the surface. As a result of which comparative catalytic activities of dissimilar crystallographic facets towards the formation of PDA and degradation of both cationic Rh B and anionic MO dyes were observed. Initially, cubic Pd seeds were synthesized as discussed above, and then different growth solutions were prepared. With the addition of Pd seeds followed by the mild reducing agent L-AA, different shapes of nanocrystals were synthesized at different temperature and time (shown in table. S1). Initially, the first synthesis was performed by maintaining the growth temperature at 45 °C with vigorous stirring up to 12 h. FESEM analysis shows that the nanocrystals were grown improperly with different shapes, and there was a lack of dispersity throughout the solution mixture, as shown in Fig. S2 (a, d). This experiment confirmed that the reaction mixture ought to remain undisturbed during the growth steps to avoid the improper growth and formation of unwanted nanocrystals. In the second experiment, there was no stirring of the growth solution keeping all the parameters constant. After 12 h of the reaction, FESEM analysis was carried out to know the change in the surface morphology. It was seen that a small yield of Pd NCs was formed in the solution along with the maximum yield of other nanocrystals given in Fig. S2 (b, e). The experiments mentioned above confirmed that undisturbed solution facilitates the deposition of metal atoms at the suitable facets producing well-grown nanocrystals. This optimization experiment noticeably discloses the importance of no disturbance during the growth step. The reaction was further optimized by changing the temperature and time to avoid the formation of unwanted nanocrystals.

In the third experiment, all the parameters were kept the same except the reaction temperature, which was increased to 60 °C. Increasing the temperature led to minimizing the formation of unwanted shapes and gave a high yield of cubes shown in Fig. S2 (c, f). Further, in the fourth experiment, raising the temperature to 70 °C resulted in the formation of well-grown Pd NCs throughout the sample. The uniform distribution, high dispersity, and clear morphology are shown in Fig. 2. However, in the fifth experiment, when the temperature was decreased to 55 °C and

growth time was increased to 13 h, a well-grown Oh morphology was observed without any other shapes. The details of the characterization of Pd Oh are shown in Fig.3. Similarly, in the sixth experiment, the temperature was additionally decreased to 35 °C and allowed to stand till 20 h to get a clear transparent growth solution. After completing the reaction time, the characterization of the solution was performed, and the formation of Pd Coh was observed as shown in Fig. 4.

From the above optimization study, it is confirmed that not only the change in the concentration of reactant, different surfactant, and external additives could alter the shapes of nanocrystals [39], but also the variation of temperature and time helps to vary the reduction rate and hence leads the formation nanocrystals. In this study, the reduction rate helps to grow different facets on the surface, showing excellent catalytic performance. Increasing the temperature leads to a fast reduction process and hence at 70 °C, a quicker reaction happens and the growth of {100} plane becomes dominant over {111} plane. The faster growth of {100} planes is due to its high surface energy compared to {111} planes [38]. The synthesis of Pd NCs, which offered excellent reactivity, was discussed in our previous work [56].
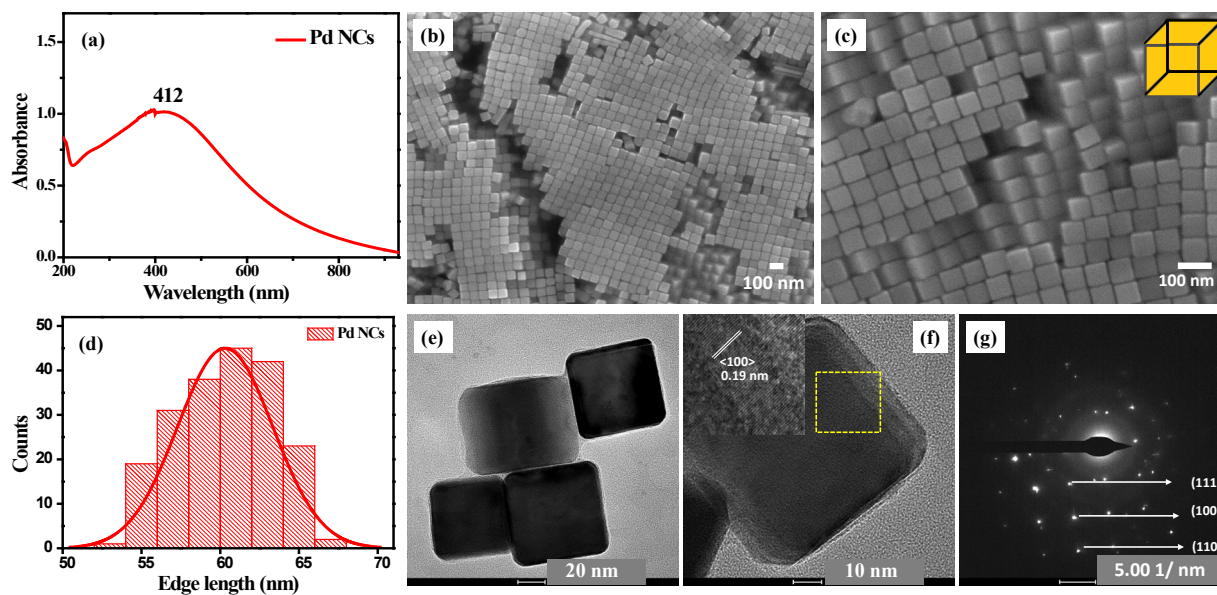

Figure 2. (a) UV-Visible spectrum of Pd NCs, (b) FESEM image Pd NCs, (c) high-resolution FESEM image Pd NCs exhibiting the monodisperse distribution throughout the sample, (d) histogram of Pd NCs, (e) TEM image of Pd NCs, (f) HRTEM image of an individual Pd NC, and (g) SAED pattern of Pd NCs.

Fig. 2 (a) represents the UV-Visible spectrum of Pd NCs of λmax 412 nm. The well-grown facets and monodispersity of Pd NCs were observed from FESEM analysis shown in Fig. 2 (b) and 2 (c), respectively. The edge length of about 60 ± 5 nm of the cubic nanocrystal was confirmed from the histogram presented in Fig. 2 (d). TEM and HRTEM images were shown in Fig. 2 (e) and 2 (f), respectively. TEM demonstrated the proper growth of facets, and growth of Pd NCs along <100> direction having d spacing 0.19 nm was confirmed from HRTEM as shown in the inset of Fig. 2 (f). The SAED pattern in Fig. 2 (g) displays the Debye-Scherrer rings corresponding to (111), (100), (110) reflection planes of Pd NCs which shows the crystallinity nature of the sample. Pd Oh was formed from the reaction mixture at 55 °C after 13 h undisturbed growth. Decreasing the temperature slows down the reduction process, and hence, the time taken to complete the growth of nanocrystals increases. The slow reduction process at the particular reaction condition blocks the exposed {100} plane on the surface, and prominent growth was directed along {111} planes resulting in octahedral structures.
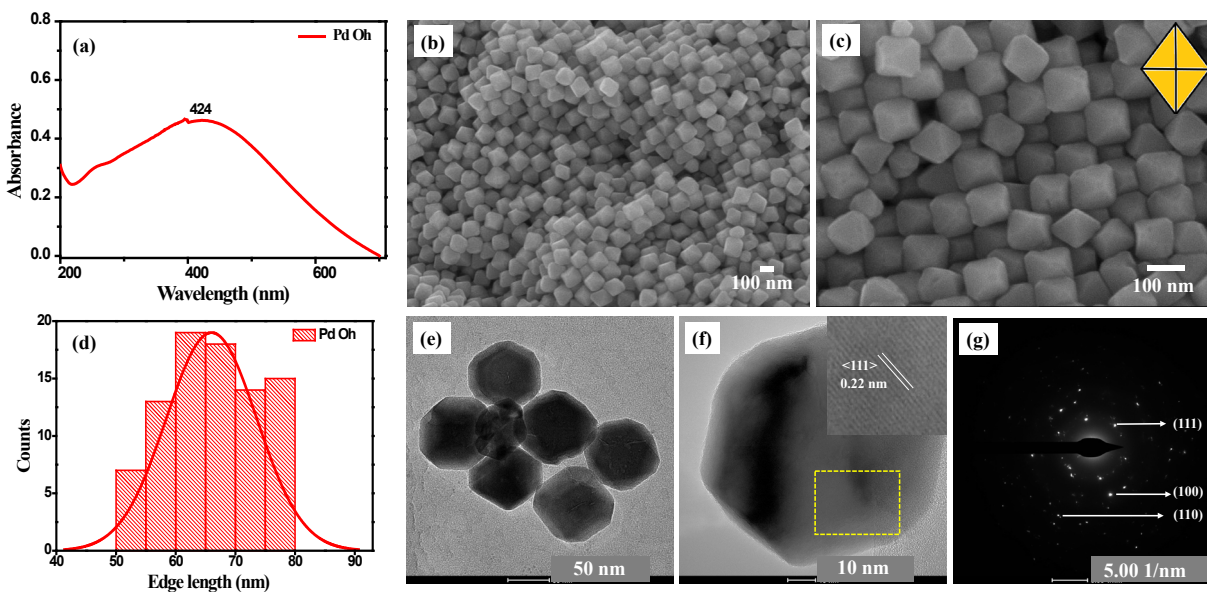

Figure 3. (a) UV-Visible spectrum of Pd Oh, (b) FESEM image Pd Oh (c) high-resolution FESEM image Pd Oh exhibiting the monodisperse distribution throughout the sample, (d) histogram of Pd Oh, (e) TEM image of Pd Oh, (f) HRTEM image of an individual Pd Oh, and (g) SAED pattern of Pd Oh.

Fig. 3 (a) represents the UV-Visible spectrum of Pd Oh exhibiting maximum absorbance at λmax 424 nm. The uniform distribution and dispersion of the desired nanostructure were confirmed from

low and high-resolution FESEM analysis, as shown in Fig. 3 (b) and 3 (c), respectively. Fig. 3 (d) displays the histogram of Pd Oh measured by edge length, and the average size was found around 65 ± 5 nm. TEM and HRTEM images showed the well-grown morphology of Pd Oh shown in Fig. 3 (e) and 3 (f), respectively. The inset of Fig. 3 (f) shows the d spacing value of 0.22 nm corresponding   to the growth along the <111> direction. The SAED pattern of Pd Oh shows (111), (100), and (110) reflection of crystalline planes of Pd is shown in Fig. 3 (g). Similarly, when the reaction was 35 °C and undisturbed up to 20 h, a slower growth rate was observed, and both the {111} and {100} planes were exposed to the surface forming Coh. UV-Visible absorption shows the characteristic peak of Pd Coh at λmax 378 nm as shown in Fig. 4 (a). Fig. 4 (b) is the FESEM image of the Coh nanocrystals confirming the monodisperse distribution throughout the sample. The average size is measured at the opposite edge length of the Coh and is found to be 50 $\pm$ 5 nm, as shown in Fig. 4 (c). HRTEM image of Pd Coh is shown in Fig. 4(d), and the inset shows the d spacing values of 0.22 and 0.19 nm corresponding to the planes of <111> and <100>, respectively. The SAED pattern in Fig. 4 (e) shows crystalline rings of Pd Coh corresponding   to (111), (100), (110) reflection planes of Coh.
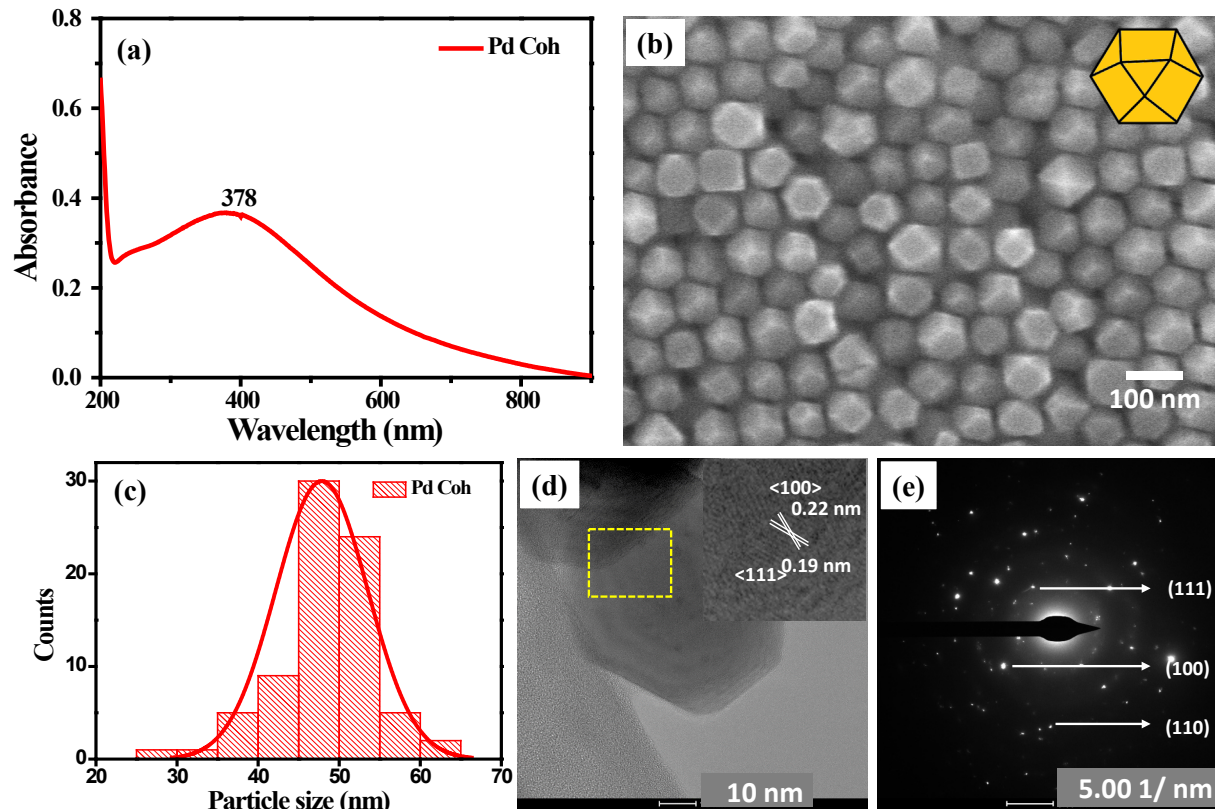
Figure 4. (a) UV-Visible spectrum of Pd Coh, (b) FESEM image Pd Coh showing Coh facet growth, (c) size distribution histogram of Pd Coh, (d) HRTEM image of an individual Pd Coh, and (e) SAED pattern of Pd Coh.

The crystalline nature of Pd nanocrystals was confirmed by PXRD analysis. The diffraction peaks at 40.1, 46.6, and 68.9 ° correspond   to (111), (200), and (220) crystal planes of Pd, respectively, mentioned in Fig. S3. All the nanocrystals had the same value of 2□□but different diffraction intensity. As a result of the growth of cubic Pd nanocrystals along the (200) plane, a high diffraction intensity was observed for the respective plane as shown in Fig. S3 (a). Whereas for Pd Oh, the intensity of (111) planes is high and for Pd Coh intensity of both (200) and (111) planes was higher than other structures shown in Fig. S3 (b) and S3 (c), respectively.

4. Application of the Pd Nanocrystals

4.1. Reduction of NA using Pd Coh, Oh, and NCs

Initially, a standard catalytic reduction process was performed by adding a light yellow colored aqueous solution of 4-NA, which shows two characteristics peaks at 230 nm and a strong absorption peak at 380 nm due to $\pi-\pi^*$ and n-π^* transition, respectively as shown in Fig. S4 (a). Control experiments were carried out to understand the role of catalyst and $NaBH_4$ in the reduction process. Time-dependent UV-Visible monitored with the addition of Pd Oh (100 μL, 1 mg/mL) catalyst without the addition of $NaBH_4$ shown in Fig. S4 (b) and Fig S4 (c) represent the addition of $NaBH_4$ without the catalyst. Interestingly, it was realized that the reduction was unable to complete in both the cases even after 4 h of the reaction and there was no conversion as shown in the spectra. Hence, it was confirmed that neither the catalyst nor $NaBH_4$ overcame the activation barrier alone to form the product [18,24]. The synthesized Pd nanocrystals (Pd Coh, Pd Oh, and Pd NCs) were prepared in the same concentration (mg/mL) to reduce the reaction. To understand the catalytic doses, firstly, 1 mg/mL Pd Oh catalyst concentration was prepared. It was found that the standard reduction reaction from 4-NA to 4-PDA required 43 min with the addition of 100 μL of catalyst, and the reduction rate value was $k = 0.6 \times 10^{-1}$ min^{-1} found from the kinetic plot between ln (C_t/C_0) Vs time (Fig. S5). As a result, a catalyst concentration of 2 mg/mL was prepared for subsequent applications. The reduction process was preliminarily observed by the addition of 100 μL of each catalyst having a different surface area. It is observed that Pd NCs facets were more reactive than Pd Oh and Pd Coh. Pd NCs completed the catalytic reduction of 4-NA in one minute,

and Pd Oh and Pd Coh in 6 and 3 min, respectively (Fig. S6). To precisely understand the catalytic activities of NCs, Oh, and Coh containing different planes/facets, the overall surface area of the particles should be unchanged (Supporting S1). Since by the addition of 100 μL of Pd NCs, the reduction proceeded very fast, further reactions were conducted by decreasing the catalyst volume to 30 μL and using the density of Pd, the volume of the entire particles in 30 μL of the Pd NCs solution was calculated by $d = \frac{m}{v}$ formula. Considering the average length of nanocrystals, the volume and surface area of a particular nanocrystal was calculated, then the mass of a specific nanocrystal was obtained. From the total volume of catalysts and volume of a single nanocrystal, the number of particles in the solution was calculated, and using the total number of catalysts, its total surface area exposed to the reduction was calculated. The calculated volume of the nanocrystal solutions was used to keep the total particle's surface area the same during the subsequent experiments (Calculation shown in S1). Keeping the surface area at about ~5 cm^2 for all three nanocrystals, different volumes were adjusted, such as 30 μL, 26.5 μL, and 15 μL of Pd NCs, Pd Oh, and Pd Coh, respectively and introduced in the solution to complete the reaction.
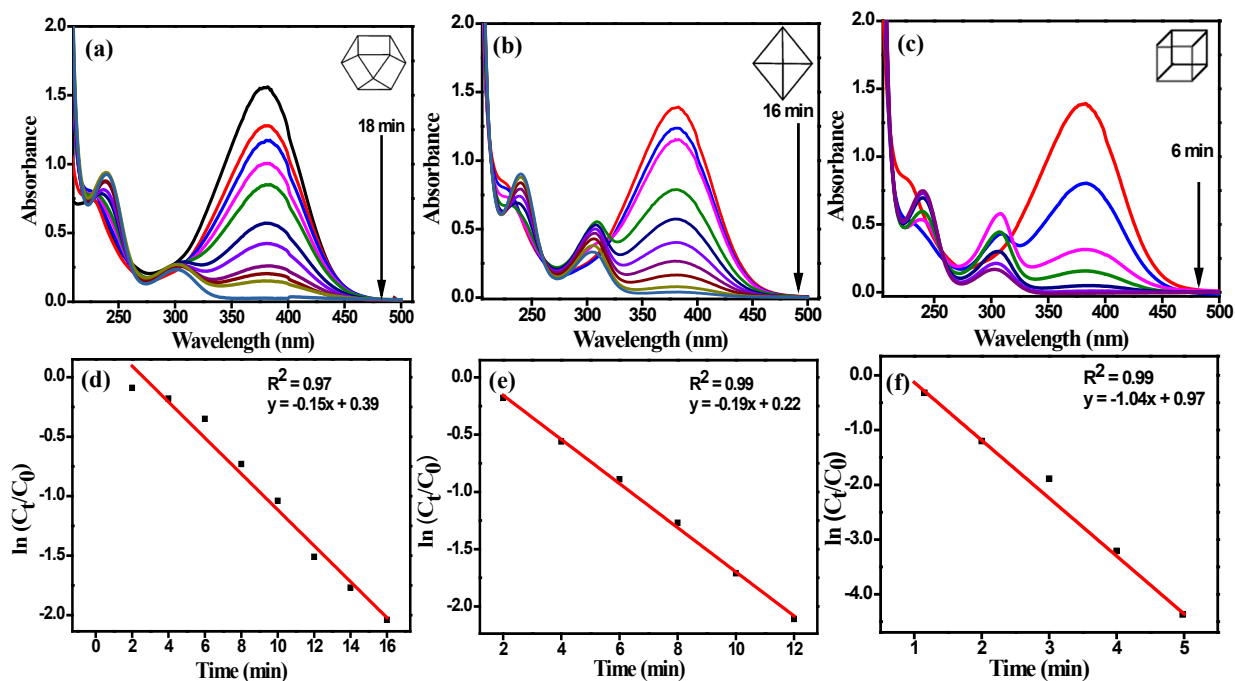

Figure 5. Representative time-dependent UV-Visible spectra of reduction of 4-NA with the addition of Pd (a) Coh, (b) Oh, and (c) NC catalysts. The kinetic plot of ln (C_t/C_0) Vs time for Pd

(d) Coh catalyst (e) Oh and (f) NCs catalyst. The concentration of catalysts was 2 mg/mL having a nearly same surface area of about 5 cm^2.

Fig. 5 (a) represents the UV-Visible spectra of reduction of 4-NA using 26.5 μL Pd Oh catalysts. Fig 5 (b) and (c) represent the reduction process of 4-NA using Pd Coh and Pd NCs catalyst, respectively. It is observed that the product formation takes place at different intervals of time for all three nanocrystals. The reduction product of 4-PDA (or benzene-1,4-diamine) demonstrates two well absorption peaks at 240 nm and another band at 305 nm signifying both π−π* and n-π* transition, respectively. The reduction process was observed by a constant decrease of the 380 nm band of 4-NA and the simultaneously slow rise of the 240 nm band of 4-PDA in the presence of a catalyst with time. In the case of Pd Coh, the time for complete reduction and 100 % product formation was achieved in 18 min, which is higher than Pd Oh and Pd NCs where the reduction time was 16 min and 6 min, respectively.
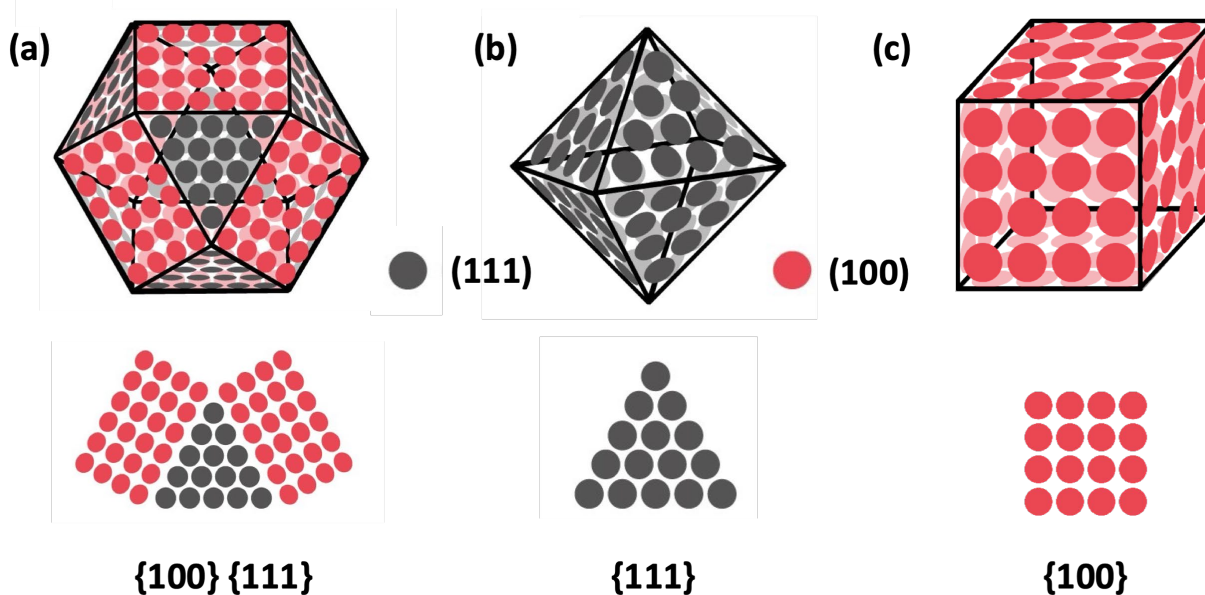

Figure 6. Schematic representation of different planes and the corresponding facets of Pd (a) Coh, (b) Oh, and (c) NCs respectively.

From 4-NP reduction performance, it was observed that Pd NCs exposing {100} facets showed the best catalytic activity compared to {111} facets of Pd Oh and Pd Coh carrying both {111} and {100} facets on the surface. The reason behind the high activity of Pd NC is due to the high surface energy associated with the surface. The {100} plane on the surface allowed more metal atom

deposition compared to the {111} plane, as shown in Fig. 6 (a). However, Oh having equilateral triangles facilitates even less deposition of active metals on the planes, as shown in Fig. 6 (b). In Coh, both the triangular and cubic faces are present having dissimilar growth and fewer metal atoms on the mutual planes are contributing to the reaction, so the activity decreases compared to Oh as shown in Fig. 6 (c). Hence, Pd NCs showed high catalytic activity followed by Oh and Coh, respectively.

To estimate the effective reaction rates of these nanocrystals, kinetic plots of $\ln(C_t/C_0)$ Vs time to reduce 4-NA are carried out with different volumes of Coh, Oh, and Pd NCs having equal surface area. To prepare the kinetic plot, absorbance values are converted to concentrations. The straight line for these data points specifies that the reduction reaction satisfies first-order kinetics. From the slope of the straight line, the rate constant k can be determined. Rate constants found for all three nanocrystals were 1.5×10^{-1}, 1.9×10^{-1}, and 10.4×10^{-1} min^{-1} for Pd Coh, Oh, and NCs as shown in Fig. 5 (d, e, f) respectively. Pd NCs catalyst which shows the best activity among all three nanocrystals exhibits a higher reaction rate than Pd Oh and Coh.
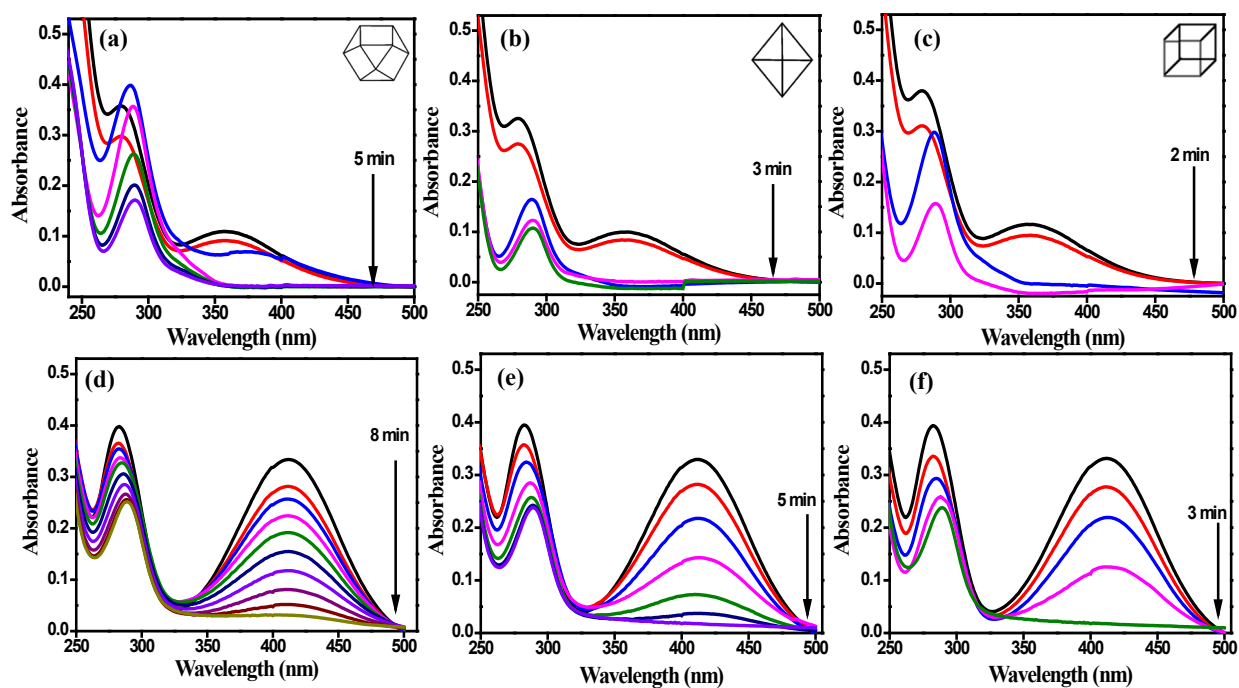

Figure 7. Represents the UV-Visible spectrum of time-dependent reduction of 3-NA using Pd (a) Coh, (b) Oh, and (c) NC catalyst. UV-Visible spectrum of time-dependent reduction of 2- NA using Pd (d) Coh (e) Oh, and (f) NC catalyst.

From the above study, it was noticed that the particle size and activity truly depend upon the nature of facets present on the surface. In present work the activity of facets follows the order Pd NCs {100}> Oh {111} > Coh {100} {111}. To understand the role of facets towards different positions of the nitro group, 3-NA and 2-NA were considered under the same condition. Fig.7 shows the time-dependent UV-Vis absorption spectra for the reduction of 3-NA and 2-NA. The dark yellow colored 3-NA displayed two absorption peaks at 278 nm and 357 nm. After the addition of $NaBH_4$ and catalysts, the peak at 357 nm decreases continuously with the rise of a new peak at 290 nm. It was observed that the time taken for reduction of 3-NA by Coh was 5 min, whereas Pd Oh and NC achieved this in 3 and 2 min, respectively, as shown in Fig. 7 (a, b, c). Similarly, 2-NA revealed two absorption peaks at 282 and 412 nm. The peak at 412 nm decreases during the reduction process, and simultaneously, a new band appears at 288 nm. The reduction time of 2-NA for all three Pd nanocrystals was 8, 5, and 3 min., corresponding to Pd Coh, Oh, and NCs, respectively as depicted in Fig. 7 (d, e, f).

Comparing all three nitro substituted anilines, it was observed that 3-NA achieved a reduction in less time followed by 2-NA and 4-NA. The reactivity trend of different NA was followed by 3-NA > 2-NA > 4-NA for all three nanocrystals. It is known that the $-NO_2$ group is an electron-withdrawing group, and hence, the reaction process is stabilized by resonance, and 2-NA is less stable than 4-NA because of steric hindrance [62]. Whereas 3-NA exhibited the least stability as there is a lack of resonance [63]. The above-mentioned reduction mechanism can proceed through a direct route and condensation route [64-66]. The more feasible route the direct route where the progress of the reaction involves the absorption of BH_4^- and the NA compound on the catalyst surface. BH_4^- serves as the electron donor in the presence of Pd nanocrystals. The aryl nitro compound is first reduced to the nitroso compound and then rapidly to the conforming hydroxylamine compound and in conclusion, the hydroxylamine compound is reduced to the required amine product [64].

4.2 Degradation of organic contaminants

The catalytic activity of Pd nanocrystals was extended further for the degradation of organic contaminant dyes such as MO and Rh B. Keeping all the parameters constant under the same atmospheric condition, degradation of both the dyes were performed. MO is used as pH indicator

and color compound in many trades in the woolen and silk industry [67]. The reductive degradation of the anionic dye, MO was started by taking the optimized catalyst amount of the same surface area and different volumes. It was noticed that the degradation occurred very fast, observed from the UV-Visible spectra, and completed within 2 min for Pd Oh and NCs and achieved in 4 min for Pd Coh as shown in Fig. S7 (a, b, c). After observing remarkable outcomes in the reductive degradation of MO, Pd nanocrystals catalysts were further promoted for the degradation of cationic dye, Rh B, to boost the catalysts' scope. The degradation process was shown for all three nanocrystals as shown in Fig. S7 (d, e, and f) for Pd Oh, Coh, and NCs, respectively. It was seen that Pd NCs took 5 min for the complete degradation of Rh B whereas Coh and Oh completed in 11 and 6 min, respectively. This confirmed the best performance of {100} planes of Pd NCs over {111} and mixed planes of both {100} and {111} on the surface.

After completion of the first NA reduction, all the nanocrystals were successfully recovered from the reaction mixture through centrifugation at 6500 rpm and washed with ethanol, followed by water two times. It was seen that the notable catalysis was completed without any change in morphology of the nanocrystals proving its consistency, robustness, and stability which is evident from Fig. S8 (a, b, c) for Pd Oh, Coh, and NCs, respectively.

5. Analytical model

5.1. Size and temperature-dependent catalytic activation energy of nanostructures

For the performance of the Pd nanocrystals with various geometries as a catalyst for different reactions, we estimated its catalytic activation energy. The catalytic activation energy depends on the geometry and electronic properties of nanoparticles. Though these two factors are interlinked, nanoparticles of the order of less than 4.2 nm are significantly influenced by electronic properties [68]. Above this, it is geometry that plays a pivotal role. This is due to the different number of atoms present on the edges and the corners. These atoms have lower coordination numbers in comparison to the atoms inside the bulk of the structure. Based on the Bond – order – Length – Strength (BOLS) correlation mechanism, these atoms have higher cohesive energy and lower electron affinity [1]. This causes higher catalytic activity. In the present study, we use an analytical approach proposed by Lu et al [69], to determine the catalytic activation energy of nanoparticles with different geometry based on a modification to spherical nanoparticles using a shape factor.

The theory is based on a size-dependent thermodynamic model for cohesive energy for spherical nanoparticles. The catalytic activation energy $E_a(D,\lambda)$ of a nanoparticle of size D is given by [69],

$$\frac{E_a(D,\lambda)}{E_a(\infty)} = \left(1 - \frac{1}{\frac{12D}{D_0} - 1}\right) exp\left(-\frac{12\lambda S_b}{3R}\frac{1}{\frac{12D}{D_0} - 1}\right) \tag{1}$$

where $E_a(\infty), D_0, \lambda, S_b$, and R are the catalytic activation energy for bulk, shape factor for different geometries of the nanoparticle, bulk solid-vapour transition entropy, critical size at which all the atoms of a crystal are located on its surface, and ideal gas constant, respectively. The solid-vapour transition entropy is obtained from the bulk enthalpy (H_b) of vaporization and boiling temperature (T_m) using the relation

$$S_b = \frac{H_b}{T_m} \tag{2}$$

The value of D_0 is equal to $6h$ where h is the atomic radius. The shape factor for a particular geometry determines the fraction of atoms present at its surface to that of a spherical nanoparticle. The fraction of atoms (δ) at the surface is given by, n/N , where n denotes the number of surface atoms and, the total number of atoms and are given by

$$N = \frac{\eta_L V_c}{V_A} \tag{3a}$$

$$n = \frac{\eta_s A_c}{A_A} \tag{3b}$$

Where the surface packing density η_s and lattice packing density η_L for standard planes like (100), (111), etc., and crystals like a face-centred cube, body centred cube are given in standard condensed matter physics textbooks. V_c, V_A, A_c, and A_A are the volume of the nanoparticle, the volume of a single atom $(\pi h^3/6)$, the surface area of the nanoparticle and surface area of a single atom $(\pi h^2/4)$, respectively. Using these, the shape factor for a particular geometry is calculated as

$$\lambda = \frac{\delta_2}{\delta_1} = \frac{n_2 N_1}{n_1 N_2} = \left(\frac{\eta_{s2}}{\eta_{s1}}\right)\left(\frac{A_{c2}}{A_{c1}}\right)\left(\frac{V_{c1}}{V_{c2}}\right) \qquad (4)$$

Where the subscript 1 and 2 represent spherical and other geometry of nanoparticles, respectively.

5.2. Shape factor for different geometries

Pd has a face-centred cubic structure and its packing density η_L is given by $\sqrt{2}\pi/6$. The shape factor for different geometries with edge length a is tabulated below in Table 1.

Table 1. Shape factor for different geometries of Pd crystal.

Geometry	η_s	A_c	V_c	Λ
Sphere with (111) facet	$\sqrt{3}\pi/6$	πa^2	$\pi a^3/6$	1
Cube with 6 (100) facets	$\pi/4$	$6a^2$	a^3	$\sqrt{3}/2$
Octahedron with 8 (111) facets	$\sqrt{3}\pi/6$	$2\sqrt{3}a^2$	$\sqrt{2}a^3/3$	$\sqrt{3/2}$
Cuboctahedron 8 (111) and 6 (100) facets	$\sqrt{3}\pi/6$ for (111) facets $\pi/4$ for (100) facets	$(6+2\sqrt{3}a^2)$	$5\sqrt{2}a^3/3$	$0.5\sqrt{3/2}$

5.3. Calculating the catalytic activation energy of Pd NCs, Oh, and Coh

The atomic radius of Pd is 0.210 nm, enthalpy of vapourization is 377.2 kJ/mol [70], boiling temperature is 2963 °C. Relative catalytic activation energy of Pd nanoparticles with a different geometry is shown in Table 2.

Table 2. Relative catalytic activation energy of Pd nanoparticles with different geometry. *The nanoparticle size D is related to the edge length a of an octahedron as $\sqrt{2}a$. Octahedron edge length is observed to be 65 nm for the present case.

Geometry	Nanoparticle size (D in nm)	Relative Catalytic activation energy $(E_a(D,\lambda)/E_a(\infty))$

NCs	60	0.9686
Oh	91.9239*	0.9719
Coh	50	0.9726

The lower the catalytic activation energy, the high is its catalytic activity. For the present nanoparticle geometries, the catalytic activation energy is in the order of NCs < Oh < Coh. Hence, the highest catalytic activity is observed for cubic particles.

6. Conclusions

To summarise, three distinct monodispersed morphologies of Pd nanocrystals with three different low index facets were synthesised via a seed-mediated synthesis protocol. At various temperatures and reaction times, CTAB acts as a surface directing agent or growth directing agent by employing L-AA as a mild reductant. A slow reduction process occurred, leading to Coh morphology at 35 °C containing {100} and {111} facets growth in 20 h. Whereas increasing the temperature resulted in the faster reduction rate and hence, at 55 °C and 70 °C Oh and NC morphologies were obtained revealing the facet growth of {111} and {100}, respectively. The Pd nanocrystals were used to analyze the standard reduction process for the conversion of 4-NA to 4-PDA, and the substituent effect of the $-NO_2$ group was also studied using 3-NA and 2-NA. To know the exact role of dissimilar facets, different amounts of catalyst volume of the same concentration were used by keeping the total particle surface area, the same. It was observed that Pd NCs exhibited the best catalytic activity, followed by Oh and Coh. After observing the exceptional performance, the catalytic activity of the nanocrystals was further extended for the degradation of cationic dye, Rh B, and anionic dye, MO, by keeping all the parameters unaltered and Pd NCs showed the best performance following the same catalytic trend. It was confirmed from the above analysis that apart from the particle size and shape, the active facets on the surface are influential for the high effectiveness of the catalyst. The catalytic action of different facets following the order {100} > {111} > {100}{111} was understood from the theoretical study. Without applying any additives, all of the produced nanocrystals demonstrated high catalytic activity for NA reduction and dye degradation and could be reused for subsequent catalytic cycles.

Notes

References

[1] S. Jiji, K. Gopchandran, Shape dependent catalytic activity of unsupported gold nanostructures for the fast reduction of 4-nitroaniline, Colloids Interface Sci. Commun. 29 (2019) 9-16.

[2] L.F. Zhang, S.L. Zhong, Xu, A.W. Rücktitelbild, Highly Branched Concave Au/Pd Bimetallic Nanocrystals with Superior Electrocatalytic Activity and Highly Efficient SERS Enhancement Angew. Chem. Int. Edit. 125 (2013) 802-802.

[3] X. Xu, Y. Li, Y. Gong, P. Zhang, H. Li, Y. Wang, Synthesis of palladium nanoparticles supported on mesoporous N-doped carbon and their catalytic ability for biofuel upgrade, J. Am. Chem. Soc. 134 (2012) 16987-16990.

[4] X. Huang, S. Tang, X. Mu, Y. Dai, G. Chen, Z. Zhou, F. Ruan, Z. Yang, N. Zheng, Freestanding palladium nanosheets with plasmonic and catalytic properties, Nat. Nanotechnol. 6 (2011) 28-32.

[5] L.M. Baldyga, S.O. Blavo, C.-H. Kuo, C.-K. Tsung, J.N. Kuhn, Size-dependent sulfur poisoning of silica-supported monodisperse Pt nanoparticle hydrogenation catalysts, ACS Catal. 2 (2012) 2626-2629.

[6] K.-L. Wu, R. Yu, X.-W. Wei, Monodispersed $FeNi_2$ alloy nanostructures: solvothermal synthesis, magnetic properties and size-dependent catalytic activity, Cryst. Eng. Comm. 14 (2012) 7626-7632.

[7] S. Panigrahi, S. Basu, S. Praharaj, S. Pande, S. Jana, A. Pal, S.K. Ghosh, T. Pal, Synthesis and size-selective catalysis by supported gold nanoparticles: study on heterogeneous and homogeneous catalytic process, J. Phys. Chem. C 111 (2007) 4596-4605.

[8] C. Zhang, S.Y. Hwang, Z. Peng, Size-dependent oxygen reduction property of octahedral Pt–Ni nanoparticle electrocatalysts, J. Mater. Chem. A 2 (2014) 19778-19787.

[9] S. Praharaj, S. Jana, S. Kundu, S. Pande, T. Pal, Effect of concentration of methanol for the control of particle size and size-dependent SERS studies, J. Colloid Interf. Sci. 333 (2009) 699-706.

[10] S. Sarkar, A.K. Sinha, M. Pradhan, M. Basu, Y. Negishi, T. Pal, Redox transmetalation of prickly nickel nanowires for morphology controlled hierarchical synthesis of nickel/gold nanostructures for enhanced catalytic activity and SERS responsive functional material, J. Phys. Chem. C 115 (2011) 1659-1673.

[11] H. Rong, S. Cai, Z. Niu, Y. Li, Composition-dependent catalytic activity of bimetallic nanocrystals: AgPd-catalyzed hydrodechlorination of 4-chlorophenol, ACS Catal. 3 (2013) 1560-1563.

[12] Q. Yuan, D.-B. Huang, H.-H. Wang, Z.-Y. Zhou, RhPt flowerlike bimetallic nanocrystals with tunable composition as superior electrocatalysts for methanol oxidation, Langmuir 30 (2014) 5711-5715.

[13] P. Wu, H. Zhang, Y. Qian, Y. Hu, H. Zhang, C. Cai, Composition-and aspect-ratio-dependent electrocatalytic performances of one-dimensional aligned Pt–Ni nanostructures, J. Phys. Chem. C 117 (2013) 19091-19100.

[14] F. Can, S.b. Berland, S.b. Royer, X. Courtois, D. Duprez, Composition-dependent performance of $Ce_xZr_{1-x}O_2$ mixed-oxide-supported WO_3 catalysts for the NOx storage reduction–selective catalytic reduction coupled process, ACS Catal. 3 (2013) 1120-1132.

[15] C. Koenigsmann, M.E. Scofield, H. Liu, S.S. Wong, Designing enhanced one-dimensional electrocatalysts for the oxygen reduction reaction: Probing size-and composition-dependent electrocatalytic behavior in noble metal nanowires, J. Phys. Chem. Lett. 3 (2012) 3385-3398.

[16] Y. Kim, H.J. Kim, Y.S. Kim, S.M. Choi, M.H. Seo, W.B. Kim, Shape-and composition-sensitive activity of Pt and PtAu catalysts for formic acid electrooxidation, J. Phys. Chem. C 116 (2012) 18093-18100.

[17] H. Bao, Z. Zhang, Q. Hua, W. Huang, Compositions, structures, and catalytic activities of $CeO_2@Cu_2O$ nanocomposites prepared by the template-assisted method. Langmuir 30 (2014) 6427-6436.

[18]   S.S.R. Gupta, M.L. Kantam, B.M. Bhanage, Shape-selective synthesis of gold nanoparticles and their catalytic activity towards reduction of p-nitroaniline, Nano-Structures & Nano-Objects 14 (2018) 125-130.

[19]   Z.-Y. Zhou, N. Tian, J.-T. Li, I. Broadwell, S.-G. Sun, Nanomaterials of high surface energy with exceptional properties in catalysis and energy storage, Chem. Soc. Rev. 40 (2011), 4167-4185.

[20]   R. Narayanan, M.A. El-Sayed, Shape-dependent catalytic activity of platinum nanoparticles in colloidal solution, Nano lett. 4 (2004) 1343-1348.

[21]   M. Shao, T. Yu, J.H. Odell, M. Jin, Y. Xia, Structural dependence of oxygen reduction reaction on palladium nanocrystals, Chem. Commun. 47 (2011) 6566-6568.

[22]   J. Wang, J. Gong, Y. Xiong, J. Yang, Y. Gao, Y. Liu, X. Lu, Z. Tang, Shape-dependent electrocatalytic activity of monodispersed gold nanocrystals toward glucose oxidation, Chem. Commun. 47 (2011) 6894-6896.

[23]   K.M. Bratlie, C.J. Kliewer, G.A. Somorjai, Structure effects of benzene hydrogenation studied with sum frequency generation vibrational spectroscopy and kinetics on Pt (111) and Pt (100) single-crystal surfaces, J. Phys. Chem. B 110 (2006) 17925-17930.

[24]   C.-Y. Chiu, P.-J. Chung, K.-U. Lao, C.-W. Liao, M.H. Huang, Facet-dependent catalytic activity of gold nanocubes, octahedra, and rhombic dodecahedra toward 4-nitroaniline reduction, J. Phys. Chem. C 116 (2012) 23757-23763.

[25]   I. Lee, R. Morales, M.A. Albiter, F. Zaera, Synthesis of heterogeneous catalysts with well shaped platinum particles to control reaction selectivity, Proc. Natl. Acad. Sci. 105 (2008) 15241-15246.

[26]   V.R. Stamenkovic, B. Fowler, B.S. Mun, G. Wang, P.N. Ross, C.A. Lucas, N.M. Marković, Improved oxygen reduction activity on Pt_3Ni (111) via increased surface site availability, Science 315 (2007) 493-497.

[27]   S. Mostafa, F. Behafarid, J.R. Croy, L.K. Ono, L. Li, J.C. Yang, A.I. Frenkel, B.R. Cuenya, Shape-dependent catalytic properties of Pt nanoparticles, J. Am. Chem. Soc. 132 (2010) 15714-15719.

[28]   R. Xu, D. Wang, J. Zhang, Y. Li, Shape-dependent catalytic activity of silver nanoparticles for the oxidation of styrene, Chem. Asian J. 1 (2006) 888-893.

[29]   N. Tian, Z.-Y. Zhou, S.-G. Sun, Y. Ding, Z.L. Wang, Synthesis of tetrahexahedral platinum nanocrystals with high-index facets and high electro-oxidation activity, Science 316 (2007) 732-735.

[30]   L. Schlapbach, A. Züttel, Hydrogen-storage materials for mobile applications Materials for Sustainable Energy, Nature 15 (2011) 265-270.

[31]   S.K. Konda, A. Chen, Palladium based nanomaterials for enhanced hydrogen spillover and storage, Mater. Today 19 (2016) 100-108.

[32]   L. Scarabelli, M. Coronado-Puchau, J.J. Giner-Casares, J. Langer, L.M. Liz-Marzan, Monodisperse gold nanotriangles: size control, large-scale self-assembly, and performance in surface-enhanced Raman scattering, ACS nano 8 (2014) 5833-5842.

[33]   M. Tebbe, M. Maennel, A. Fery, N. Pazos-Perez, R.A. Alvarez-Puebla, Organized solid thin films of gold nanorods with different sizes for surface-enhanced Raman scattering applications, J. Phys. Chem. C 118 (2014) 28095-28100.

[34]   J.F. Li, Y.F. Huang, Y. Ding, Z.L. Yang, S.B. Li, X.S. Zhou, F.R. Fan, W. Zhang, Z.Y. Zhou, B. Ren, Shell-isolated nanoparticle-enhanced Raman spectroscopy, Nature 464 (2010) 392-395.

[35]   (a) Z.-Q. Tian, B. Ren, Adsorption and reaction at electrochemical interfaces as probed by surface-enhanced Raman spectroscopy, Annu. Rev. Phys. Chem. 55 (2004) 197-229. (b) Z.-Q. Tian, B. Ren, J.-F. Li, Z.-L. Yang, Expanding generality of surface-enhanced Raman spectroscopy with borrowing SERS activity strategy. Chem. Commun. 34 (2007) 3514-3534.

[36]   A. Klinkova, A. Ahmed, R.M. Choueiri, J.R. Guest, E. Kumacheva, Toward rational design of palladium nanoparticles with plasmonically enhanced catalytic performance, RSC Adv. 6 (2016) 47907-47911.

[37]   W. Niu, Z.-Y. Li, L. Shi, X. Liu, H. Li, S. Han, J. Chen, G. Xu, Seed-mediated growth of nearly monodisperse palladium nanocubes with controllable sizes, Cryst. Growth Des. 8 (2008) 4440-4444.

[38]   Y. Xia, X. Xia, H.-C. Peng, Shape-controlled synthesis of colloidal metal nanocrystals: thermodynamic versus kinetic products, J. Am. Chem. Soc. 137 (2015) 7947-7966.

[39]   H. Zhang, M. Jin, Y. Xiong, B. Lim, Y. Xia, Shape-controlled synthesis of Pd nanocrystals and their catalytic applications, Acc. Chem. Res. 46 (2013) 1783-1794.

[40]   T.S. Ahmadi, Z.L. Wang, T.C. Green, A. Henglein, M.A. El-Sayed, Shape-controlled synthesis of colloidal platinum nanoparticles, Science 272 (1996) 1924-1925.

[41]   B. Wiley, Y. Sun, Y. Xia, Synthesis of silver nanostructures with controlled shapes and properties, Acc. Chem. Res. 40 (2007) 1067-1076.

[42]   B. Lim, Xiong, Y. Y. Xia, A water-based synthesis of octahedral, decahedral, and icosahedral Pd nanocrystals, Angew. Chem. 119 (2007) 9439-9442.

[43]   M. Jin, H. Liu, H. Zhang, Z. Xie, J. Liu, Y. Xia, Synthesis of Pd nanocrystals enclosed by {100} facets and with sizes < 10 nm for application in CO oxidation, Nano Res. 4 (2011) 83-91.

[44]   Y. Xiong, H. Cai, B.J. Wiley, J. Wang, M.J. Kim, Y. Xia, Synthesis and mechanistic study of palladium nanobars and nanorods, J. Am. Chem. Soc. 129 (2007) 3665-3675.

[45]   B. Lim, H. Kobayashi, P.H. Camargo, L.F. Allard, J. Liu, Y. Xia, New insights into the growth mechanism and surface structure of palladium nanocrystals, Nano Res. 3 (2010) 180-188.

[46]   H. Duan, H. Wang, W. Huang, Influence of Polyvinylpyrrolidone Capping Ligands on Electrocatalytic Oxidation of Methanol and Ethanol over Palladium Nanocrystal Electrocatalysts, Acta. Phys. Chim. Sin. 37 (2021) 200305.

[47]   M. Jin, H. Zhang, Z. Xie, Y. Xia, Palladium nanocrystals enclosed by {100} and {111} facets in controlled proportions and their catalytic activities for formic acid oxidation, Energy Environ. Sci. 5 (2012) 6352-6357.

[48]   W. Niu, L. Zhang, G. Xu, Shape-controlled synthesis of single-crystalline palladium nanocrystals, ACS nano 4 (2010) 1987-1996.

[49]   C. Zlotea, F. Cuevas, V. Paul-Boncour, E. Leroy, P. Dibandjo, R. Gadiou, C. Vix-Guterl, M. Latroche, Size-dependent hydrogen sorption in ultrasmall Pd clusters embedded in a mesoporous carbon template, J. Am. Chem. Soc. 132 (2010) 7720-7729.

[50]   A.I. Ayad, C.B. Marín, E. Colaco, C. Lefevre, C. Méthivier, A.O. Driss, J. Landoulsi, E. Guénin, "Water soluble" palladium nanoparticle engineering for C–C coupling, reduction and cyclization catalysis, Green Chem. 21 (2019) 6646-6657.

[51]   B. Yuan, Y. Pan, Y. Li, B. Yin, H. Jiang, A highly active heterogeneous palladium catalyst for the Suzuki–Miyaura and Ullmann coupling reactions of aryl chlorides in aqueous media, Angew. Chem. Int. Edit. 49 (2010) 4054-4058.

[52]   A. Balanta, C. Godard, C. Claver, Pd nanoparticles for C–C coupling reactions, Chem. Soc. Rev. 40 (2011) 4973-4985.

[53]   A. Fihri, M. Bouhrara, B. Nekoueishahraki, J.-M. Basset, V. Polshettiwar, Nanocatalysts for Suzuki cross-coupling reactions, Chem. Soc. Rev. 40 (2011) 5181-5203.

[54]   F. Wang, C. Li, L.D. Sun, C.H. Xu, J. Wang, J.C. Yu, C.H. Yan, Porous single-crystalline palladium nanoparticles with high catalytic activities, Angew. Chem. 124 (2012) 4956-4960.

[55]   M. Laskar, S.E. Skrabalak, Decoupling the geometric parameters of shape-controlled Pd nanocatalysts, ACS Catal. 4 (2014) 1120-1128.

[56]   S. Swain, B. MB, V. Kandathil, P. Bhol, A.K. Samal, S.A. Patil, Controlled Synthesis of Palladium Nanocubes as an Efficient Nanocatalyst for Suzuki–Miyaura Cross-Coupling and Reduction of p-Nitrophenol, Langmuir 36 (2020) 5208-5218.

[57]   J. Yin, B. Ge, T. Jiao, Z. Qin, M. Yu, L. Zhang, Q. Zhang, Q. Peng, Self-assembled sandwich-like MXene-derived composites as highly efficient and sustainable catalysts for waste water treatment, Langmuir 37 (2021) 1267-1278.

[58]   H. Deng, J. Yin, J. Ma, J. Zhou, L. Zhang, L. Gao, T. Jiao, Exploring the enhanced catalytic performance on nitro dyes via a novel template of flake-network Ni-Ti LDH/GO in-situ deposited with Ag_3PO_4 NPs, Appl. Surf. Sci. 543 (2021) 148821.

[59]   J. Zhu, X. Zhang, Z. Qin, L. Zhang, Y. Ye, M. Cao, L. Gao, T. Jiao, Preparation of PdNPs doped chitosan-based composite hydrogels as highly efficient catalysts for reduction of 4-nitrophenol. Colloids Surf. A 611 (2021) 125889.

[60]   C. Qian, J. Yin, J. Zhao, X. Li, S. Wang, Z. Bai, T. Jiao, Facile preparation and highly efficient photodegradation performances of self-assembled Artemia eggshell-ZnO nanocomposites for wastewater treatment. Colloids Surf. A 610 (2021) 125752.

[61]   H. Zhao, R. Wang, H. Deng, L. Zhang, L. Gao, L. Zhang, T. Jiao, Facile Preparation of Self-Assembled Chitosan-Based POSS-CNTs-CS Composite as Highly Efficient Dye Absorbent for Wastewater Treatment. ACS Omega 6 (2020) 294-300.

[62]   S. Wunder, F. Polzer, Y. Lu, Y. Mei, M. Ballauff, Kinetic analysis of catalytic reduction of 4-nitrophenol by metallic nanoparticles immobilized in spherical polyelectrolyte brushes, J. Phys. Chem. C 114 (2010) 8814-8820.

[63]   T. Aditya, J. Jana, N.K. Singh, A. Pal, T. Pal, Remarkable facet selective reduction of 4-nitrophenol by morphologically tailored (111) faceted Cu_2O nanocatalyst, ACS omega 2 (2017) 1968-1984.

[64]   S. Kundu, S. Lau; H. Liang, Shape-controlled catalysis by cetyltrimethylammonium bromide terminated gold nanospheres, nanorods, and nanoprisms, J. Phys. Chem. C 113 (2009), 5150-5156.

[65]   K. Layek, M.L. Kantam, M. Shirai, D. Nishio-Hamane, T. Sasaki, H. Maheswaran, Gold nanoparticles stabilized on nanocrystalline magnesium oxide as an active catalyst for reduction of nitroarenes in aqueous medium at room temperature, Green Chem. 14 (2012), 3164-3174.

[66]   X.B. Lou, L. He, Y. Qian, Y.M. Liu, Y. Cao, K.N. Fan, Highly Chemo-and Regioselective Transfer Reduction of Aromatic Nitro Compounds using Ammonium Formate Catalyzed by Supported Gold Nanoparticles, Advan. Synth. Catal. 353 (2011) 281-286.

[67]   M. Roy, A. Mondal, A. Mondal, A. Das, D. Mukherjee, Polyaniline Supported Palladium Catalyzed Reductive Degradation of Dyes Under Mild Condition. Current Green Chem. 6 (2019) 69-75.

[68]   Hengwei: Gu Wang, Kui; Zheng Xiang, Pan Xusheng, Zhu Haibin, Chen Junfa, Cao Si, Li Lina, Xue Wei, Junling Lu, Disentangling the size-dependent geometric and electronic effects of palladium nanocatalysts beyond selectivity, Sci. Adv. 5 (2019) eaat6413.

[69]   H. Lu, X. Meng, Theoretical model to calculate catalytic activation energies of platinum nanoparticles of different sizes and shapes, J. Phys. Chem. C 114 (2010) 1534-1538.

[70]   S.R Bharadwaj, A.S Kerkar, S.N Tripathi, R. Kameswaran, Vapourization study of pure Palladium, J. Chem. Thermodyn. 22 (1990) 453-461.